Letter | Editors' Suggestion

Direct visualization and control of antiferromagnetic domains and spin reorientation in a parent cuprate

K. L. Seyler,[1,2] A. Ron,[1,2,3] D. Van Beveren,[1,2] C. R. Rotundu,[4] Y. S. Lee,[4,5] and D. Hsieh[1,2]

[1]*Department of Physics, California Institute of Technology, Pasadena, California 91125, USA*

[2]*Institute for Quantum Information and Matter, California Institute of Technology, Pasadena, California 91125, USA*

[3]*Raymond and Beverly Sackler School of Physics and Astronomy, Tel-Aviv University, Tel Aviv, 69978, Israel*

[4]*Stanford Institute for Materials and Energy Sciences, SLAC National Accelerator Laboratory, 2575 Sand Hill Road, Menlo Park, California 94025, USA*

[5]*Department of Applied Physics, Stanford University, Stanford, California 94305, USA*

(Received 1 July 2022; revised 24 August 2022; accepted 4 October 2022; published 12 October 2022)

We report magnetic optical second-harmonic generation (SHG) polarimetry and imaging on $Sr_2Cu_3O_4Cl_2$, which allows direct visualization of the mesoscopic antiferromagnetic (AFM) structure of a parent cuprate. Temperature- and magnetic-field-dependent SHG reveals large domains with 90° relative orientations that are stabilized by a combination of uniaxial magnetic anisotropy and the Earth's magnetic field. Below a temperature $T_R \sim 97$ K, we observe an unusual 90° spin-reorientation transition, possibly driven by competing magnetic anisotropies of the two copper sublattices, which swaps the AFM domain states while preserving the domain structure. This allows deterministic switching of the AFM states by thermal or laser heating. Near T_R, the domain walls become exceptionally responsive to an applied magnetic field, with the Earth's field sufficient to completely expel them from the crystal. Our findings unlock opportunities to study the mesoscopic AFM behavior of parent cuprates and explore their potential for AFM technologies.

DOI: 10.1103/PhysRevB.106.L140403

Antiferromagnetic (AFM) materials host a rich variety of magnetic phenomena and are appealing for robust high-speed spin-based technologies [1–4]. Cuprate Mott insulators, the parent compounds of high-T_c superconductors, are particularly intriguing AFM materials owing to their model Heisenberg behavior, record-high exchange interactions, and tunability with doping [5,6]. However, there is limited understanding of their mesoscopic magnetic properties due to the difficulty of achieving local readout of AFM order and spatial mapping of AFM domain wall distributions [7,8]. Here we directly visualize AFM domains in the parent cuprate $Sr_2Cu_3O_4Cl_2$ using optical second-harmonic generation (SHG) polarimetry and imaging. We uncover a spin-reorientation transition that enables thermally controlled deterministic 90° switching of AFM states and complete expulsion of AFM domain walls with Oersted-level magnetic fields.

Magnetic crystals that break time-reversal symmetry permit time-noninvariant (*c*-type) SHG processes that directly couple to the magnetic order parameter [9,10], making SHG a potentially powerful probe of AFM domains [9,11] and dynamics [12]. Although *c*-type SHG is most widely reported in the electric-dipole channel from noncentrosymmetric AFM materials [13–16], it has also been detected in weaker magnetic-dipole (MD) channels from centrosymmetric materials [17,18]. However, ideal AFM-ordered parent cuprates preserve time-reversal symmetry because even though time reversal is locally broken at each Cu site, it is restored upon translation by a primitive lattice vector. This leads to perfect cancellation of *c*-type SHG radiation from the two magnetic sublattices. Therefore, cuprate antiferromagnetism is expected to be SHG inactive, as was recently confirmed in the prototypical compound $Sr_2CuO_2Cl_2$ [19,20].

The centrosymmetric tetragonal structure (point group, $4/mmm$) of $Sr_2Cu_3O_4Cl_2$ is nearly identical to $Sr_2CuO_2Cl_2$ except for an additional set of Cu^{2+} ions (Cu_{II}) located in every other plaquette of the conventional CuO_2 lattice [Cu_I, Fig. 1(a)] [21]. The Cu_I spins interact via strong intralayer AFM exchange ($J_I = 130$ meV) and order below $T_{N,I} \approx 380$ K, well above the AFM ordering temperature of the Cu_{II} sublattice ($T_{N,II} \approx 40$ K) [22]. However, because Cu_{II} breaks the equivalence of neighboring Cu_I sites, the AFM-ordered Cu_I sublattice becomes SHG active below $T_{N,I}$. The AFM-ordered Cu_I sublattice generates a net field at the Cu_{II} sites via a weak pseudodipolar interaction [23,24]. This induces a polarization of Cu_{II} spins and slight canting of Cu_I spins, resulting in a centrosymmetric AFM structure (point group $mm'm'$) with a small net in-plane ferromagnetic moment **M** [23,24] [Fig. 1(a)]. Four degenerate 90°-rotated AFM domain configurations correspond to **M** along [110], [$\bar{1}$10], [$\bar{1}\bar{1}$0], or [1$\bar{1}$0], which can in principle be distinguished via MD SHG. A previous study used bulk magnetometry to infer the existence of stable AFM domains with 90° relative orientations and a domain wall phase transition near 100 K [7], where it was proposed that domains are stabilized by entropic [7] or magnetoelastic [25] effects. However, direct observation of AFM domains has remained elusive.

To establish the existence of an SHG response that directly couples to the magnetic order parameter, which can be represented by **M**, we performed rotational anisotropy

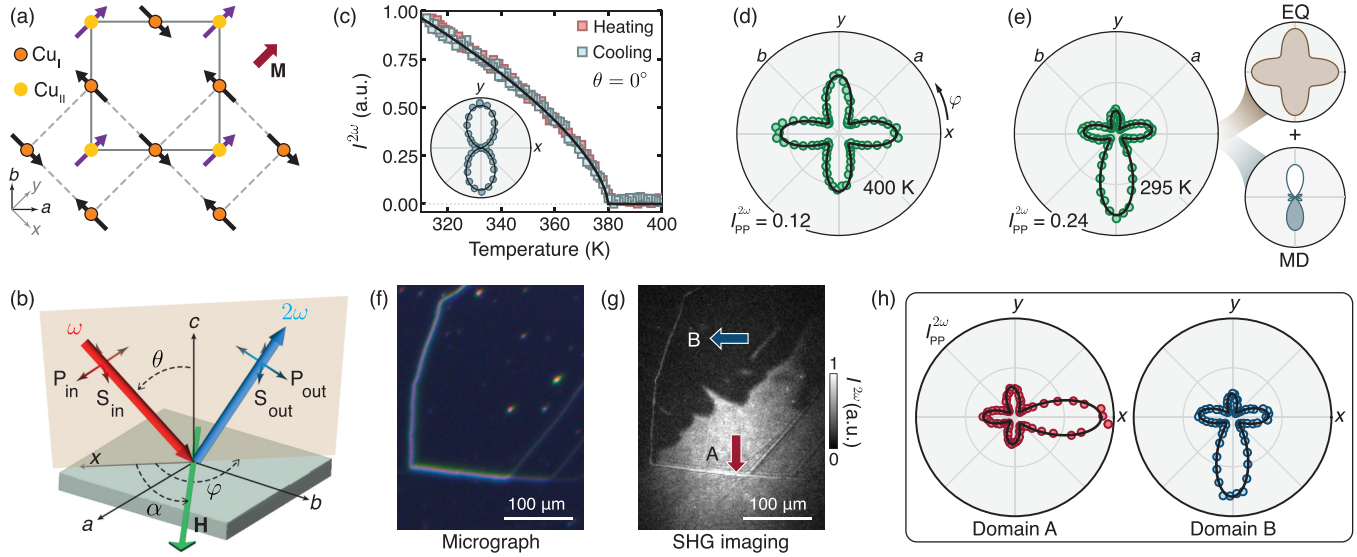

FIG. 1. Local AFM readout in $Sr_2Cu_3O_4Cl_2$. (a) Crystal and magnetic structure of single Cu-O layer in $Sr_2Cu_3O_4Cl_2$. Only the moment induced by internal pseudodipolar field is depicted. Thick arrow indicates **M**. (b) Schematic of RA-SHG experimental geometry, where angle of incidence (θ), scattering plane angle (φ), in-plane magnetic field (**H**) direction (α), and input and output electric field polarizations (P or S) are varied. (c) Temperature dependence of normal incidence ($\theta = 0°$) SHG intensity. Solid line is a least-squares fit to $I^{2\omega} \propto (T_{N,I} - T)^{2\beta}$, where $\beta = 0.32(3)$ and $T_{N,I} = 380(1)$ K. Fit is performed near $T_{N,I}$ (360 K $\leqslant T \leqslant$ 380 K) with uncertainties given as 1 standard deviation. Inset: normal incidence RA-SHG for colinearly polarized excitation and detection beams measured at $T = 295$ K and fit by $\chi^{MD(c)}$ ($mm'm'$) process (solid line). (d) Oblique-incidence ($\theta = 10°$) P$_{in}$-P$_{out}$ RA-SHG pattern at 400 K fit by a $\chi^{EQ(i)}$ ($4/mmm$) process (solid line). (e) P$_{in}$-P$_{out}$ RA-SHG pattern ($\theta = 10°$) at 295 K fit to a coherent superposition of $\chi^{EQ(i)}$ ($4/mmm$) and $\chi^{MD(c)}$ ($mm'm'$) processes. EQ and MD processes are illustrated on the right, where patterns represent the P$_{in}$-light-induced nonlinear polarization projected along P$_{out}$. Filled and white lobes indicate opposite phase. (f) Dark-field optical micrograph of cleaved (001) $Sr_2Cu_3O_4Cl_2$. Bright and dark lines correspond to surface terrace steps. (g) Wide-field SHG image under horizontal excitation polarization (along x axis) at 295 K. Domains A and B are labeled with arrow corresponding to **M**. (h) P$_{in}$-P$_{out}$ RA-SHG patterns at 295 K for domains A and B.

(RA) measurements on (001)-cleaved single crystals of $Sr_2Cu_3O_4Cl_2$ using a fast-rotating scattering-plane-based technique [Fig. 1(b)] [26]. Under normal incidence ($\theta = 0°$), a nonzero SHG signal appears below $T_{N,I}$ and shows no thermal hysteresis [Fig. 1(c)], consistent with a continuous AFM transition. The dumbbell-shaped RA patterns are well described by a magnetization-induced MD process $P_i^{2\omega} = \chi_{ijk}^{MD(c)} E_j^{\omega} H_k^{\omega}$, where $\chi_{ijk}^{MD(c)}$ is an axial c-type susceptibility tensor respecting $mm'm'$ symmetry [27] that relates the incident electric and magnetic fields at frequency ω to the induced polarization at 2ω, and the subscripts run through x, y, and z. Below $T_{N,I}$, $\chi^{MD(c)}$ exhibits a power-law temperature dependence with a fitted critical exponent $\beta = 0.32(3)$, which is consistent with the critical exponent of the staggered and saturated moments measured by neutron diffraction [22,32] and magnetometry [23,24] to within experimental errors. Together, these data confirm a $\chi_{ijk}^{MD(c)}$ response that scales linearly with **M**. To determine the sign of $\chi_{ijk}^{MD(c)}$, we measured RA patterns at oblique incidence ($\theta = 10°$), where a temperature-independent time-invariant (i-type) electric quadrupole (EQ) SHG process becomes active [Fig. 1(d)]. Below $T_{N,I}$, the EQ and MD terms interfere to produce an RA pattern with broken rotational symmetry, revealing the sign of $\chi_{ijk}^{MD(c)}$ [Fig. 1(e), [27]]. All four AFM domain configurations can therefore be locally read out from the orientation of the large lobe in the RA pattern.

A typical white light image of cleaved $Sr_2Cu_3O_4Cl_2$ shows a smooth surface except for a few lines from cleavage terraces [Fig. 1(f)]. Contrast between 90° AFM domains is achieved using wide-field polarized SHG imaging at normal incidence. Under horizontal excitation polarization [27], regions with **M** along the $\pm y$ ($\pm x$) direction appear bright (dark). An SHG image captured over the same field of view at $T = 295$ K shows clear bright and dark regions spanning hundreds of microns [Fig. 1(g)]. By collecting oblique incidence RA patterns at different locations throughout the imaged area [Fig. 1(h)], we find that the entire bright (dark) region corresponds to a single AFM domain with **M** oriented along $-y$ ($-x$). The realization of only two out of four possible domain orientations is observed across multiple crystals. By repeating these measurements following multiple thermal cycles across $T_{N,I}$ and under different orientations of the crystal in the laboratory frame, we report two main phenomena [27]. First, the location of 90° domain walls is largely reproducible, suggesting pinning to structural features. Second, the direction of **M** within the bright (dark) domain is fixed along either the $+y$ ($+x$) direction or the $-y$ ($-x$) direction, depending on the orientation of the crystal relative to the Earth's magnetic field. Antiphase domains with 180° walls are removed even by the weak field of Earth upon cooling below $T_{N,I}$. These observations suggest that a particular AFM configuration is selected through an interplay of the Earth's field with an underlying

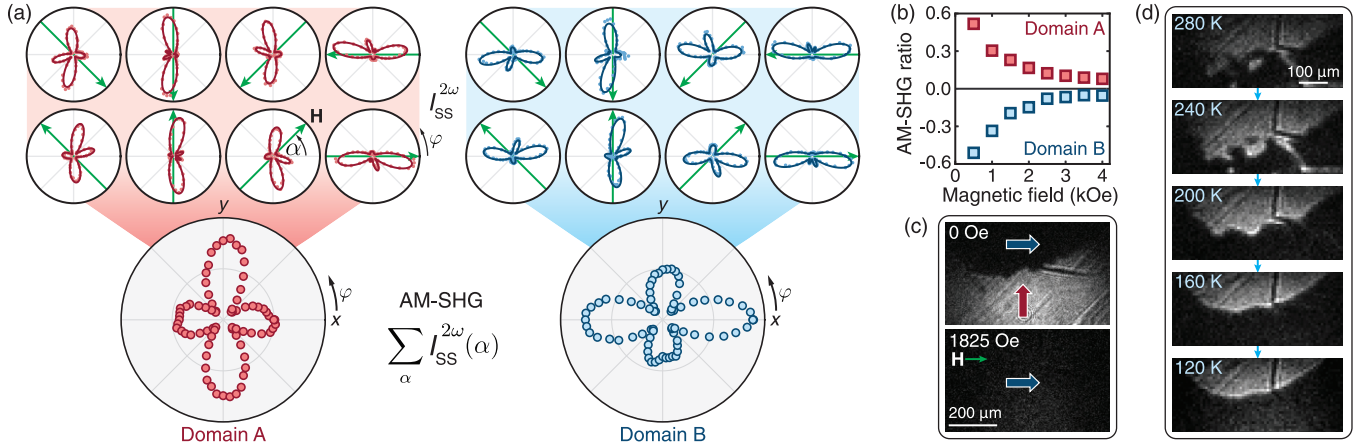

FIG. 2. Evidence for uniaxial in-plane anisotropy. (a) S_{in}-S_{out} RA-SHG patterns at 295 K on domains A and B with $|H| = 1$ kOe for different α (from 0° to 315° in 45° steps). AM-SHG pattern (bottom) is produced by summing all eight RA patterns. (b) $|H|$-dependence of AM-SHG ratio on each domain, defined as $(I_y^{sum} - I_x^{sum})/I_{min}^{sum}$, where $I_x^{sum}(I_y^{sum})$ are AM-SHG lobe intensities along x (y) and I_{min}^{sum} is the smaller of I_x^{sum} or I_y^{sum}. Higher absolute ratio values correspond to larger deviation from C_4 symmetry. (c) SHG images at $H = 0$ Oe (top) and $H = 1825$ Oe (bottom) at 295 K under horizontal excitation polarization. H-field and magnetization directions are indicated by arrows. (d) SHG images showing 90° domain wall temperature dependence. Dark lines correspond to terrace steps. Acquired with vertical polarization.

uniaxial magnetic anisotropy along the y (x) axis in the bright (dark) domain.

The presence of uniaxial anisotropy can be probed using anisotropic magneto-SHG (AM-SHG), where RA patterns are measured under different applied in-plane magnetic field (**H**) directions (α) [33]. Figure 2(a) shows S_{in}-S_{out} RA patterns from two 90° domains for different α with $H = 1$ kOe. The AM-SHG patterns, obtained by summing RA patterns over α, exhibit a clear twofold-rotational symmetry (C_2) characteristic of uniaxial anisotropy [Fig. 2(a)], with the axis differing by 90° for the two domains. These data confirm the presence of a domain-dependent in-plane uniaxial magnetic anisotropy. A low field was necessary for this measurement because for $H > 3$ kOe, a spin-rotation transition occurs for **H** along ⟨100⟩ [23,24], which obscures the C_2 contribution to the AM-SHG patterns [Fig. 2(b)]. Field-dependent SHG imaging shows that a domain can be reoriented by 90° at sufficiently high H [Fig. 2(c)], which appears to occur through the growth and merger of smaller domains [27]. Combined with the thermal cycling results, the data suggest that the structural symmetry is lower than tetragonal above $T_{N,I}$. Structural domains may arise from previously unresolved high-temperature orthorhombic distortions, which impose spatially nonuniform uniaxial anisotropy below $T_{N,I}$. The system may also be subject to extrinsic stresses from crystallographic defects as well as intrinsic stresses that are expected to accompany AFM order in finite crystals [25,27].

The AFM domain distribution is dictated primarily by competition between the uniaxial anisotropy and Cu_I-Cu_I spin-exchange energies. Although anisotropy is much weaker than exchange [27], a 90° AFM domain wall can nevertheless form along structural domain boundaries because the exchange energy cost scales with the wall area, whereas the anisotropy energy saved scales with the domain volume. Just below $T_{N,I}$, we observe fragmentary AFM domains with rough edges [Fig. 2(d)], likely conforming to an underlying distribution of structural domains. Upon further cooling, fragments merge to form larger AFM domains with smoother walls, indicating an increasing exchange contribution relative to the anisotropy that is possibly driven by changes in the ordered moment magnitude and temperature-dependent anisotropy. From 160 to 100 K, the domain boundaries remain largely stable. This general trend is consistent across multiple samples [27].

Figure 3(a) shows the evolution of a typical 90° AFM domain upon further cooling below 100 K. Remarkably, within 1 K around $T_R = 97$ K, the domain wall is rapidly expelled from the sample, realizing a global single-domain state, and then reappears and snaps back into its original position with swapped bright and dark regions. This behavior is completely reversible upon re-heating through T_R with slight thermal hysteresis. Local RA measurements confirm that **M** reorients by 90° within each domain across T_R, with the two domains effectively swapping **M**. While a previous study observed magnetization anomalies and inferred changes in relative domain sizes in this temperature regime [7], the domain reorientation at T_R has remained hidden until this work. This reorientation transition enables repeated deterministic 90° switching of the local AFM order parameter simply by cycling the cryostat temperature through T_R [Fig. 3(b)], or by fixing the cryostat temperature below T_R and changing the optical power [Fig. 3(c)].

The AM-SHG pattern from a single AFM domain has C_2 symmetry just above T_R, becomes C_4 at T_R, and then recovers a C_2 form below T_R that is 90° rotated from the high-temperature pattern [Fig. 3(d)]. This strongly suggests that the reorientation transition is driven by a change in sign of the uniaxial magnetic anisotropy at T_R. In Fig. 3(e), we propose a simple microscopic picture in which Cu_I and Cu_{II} spins exhibit temperature-dependent in-plane uniaxial magnetic anisotropies (K_I and K_{II}). An expression for the anisotropy energy of a single domain is $E(T) = E_0 + [2K_I(T) - K_{II}(T)]\sin^2\psi - K_4\cos(4\psi)$, where ψ is the angle between **M** and the $+x$ direction, and K_4

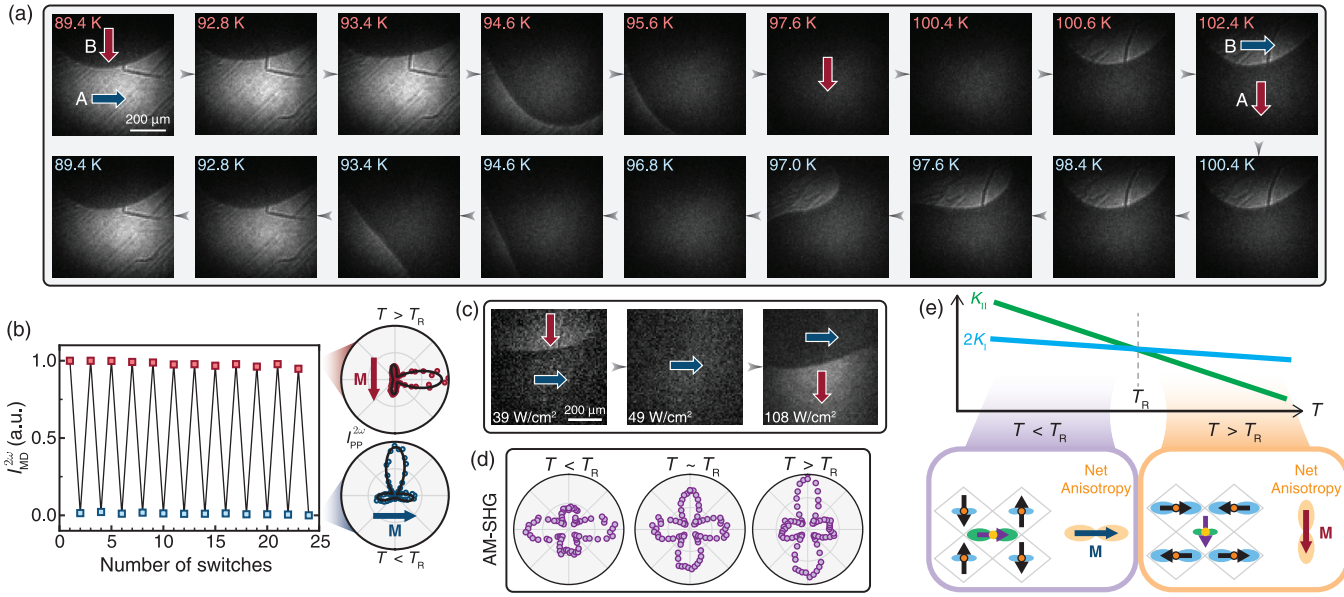

FIG. 3. Thermally driven domain reorientation transition. (a) SHG images acquired at select temperatures upon warming (top) and cooling (bottom). Arrows indicate **M**. Excitation was vertically polarized. Similar behavior was confirmed in a second sample [27]. (b) MD SHG intensity on domain A under repeated thermal switching through heating to 120 K (red) and cooling to 80 K (blue). Corresponding P_{in}-P_{out} patterns shown on right. (c) SHG images acquired at three different excitation intensities for 95.5 K. (d) AM-SHG patterns acquired at $T_R - 10$ K, T_R, and $T_R + 5$ K with $H = 1180$ Oe from a single domain. (e) Schematic of competing magnetic anisotropies model. The graph depicts how Cu_I and Cu_{II} in-plane spin anisotropies, labeled as K_I and K_{II}, respectively, may vary around T_R. The factor of 2 in front of K_I arises because there are twice as many Cu_I as Cu_{II} per unit cell. In the crystal schematics, blue (green) lobe sizes and orientations depict the direction and strength of Cu_I (Cu_{II}) spin anisotropy above and below T_R for domain A. Domain B is similar but rotated by 90°.

is a biaxial anisotropy term [23,24,34]. The Cu_I and Cu_{II} spins prefer a relative orientation of 90°. If K_I and K_{II} have the same sign but different strength [depicted by blue and green lobes in Fig. 3(e)], the two terms compete, with the larger of $2K_I$ and K_{II} determining the sign of the net uniaxial anisotropy and resulting orientation of **M**. We hypothesize that K_I and K_{II} exhibit different temperature dependencies and cross at T_R, driving the 90° AFM reorientation. Since Cu_I and Cu_{II} lie at nonequivalent lattice sites, it is reasonable that a distortion-dependent single-ion anisotropy [35] will differ for each ion in both its strength and temperature dependence. The uniaxial anisotropy may also microscopically involve two-ion terms such as anisotropic exchange and magnetic dipole-dipole coupling, which is beyond the scope of this work to disentangle. We further note that spin correlations within the Cu_{II} sublattice have been shown to onset near $T = 100$ K [32], potentially inducing magnetoelastic deformations.

This phenomenon is reminiscent of the transition across the isotropic point of Fe_3O_4 [36,37] and the Morin transition of α-Fe_2O_3 [38]. In these cases, spin reorientation occurs when temperature-dependent anisotropy contributions, originating from different magnetic ions or anisotropy mechanisms [39,40], compensate one another to drive an anisotropy term across zero [41]. Our observations in $Sr_2Cu_3O_4Cl_2$ are distinguished from other temperature-dependent spin-reorientation transitions in that the domain distribution is preserved, with the underlying distortions holding a memory of the domain structure while the anisotropy sets the spin orientation. Moreover, in $Sr_2Cu_3O_4Cl_2$, the transition has been difficult to discern using bulk-averaged probes because it involves domain-dependent spin reorientation as opposed to a global change in easy axis.

Near T_R, the AFM domain walls become exceptionally responsive to small H. Figure 4(a) illustrates the change in

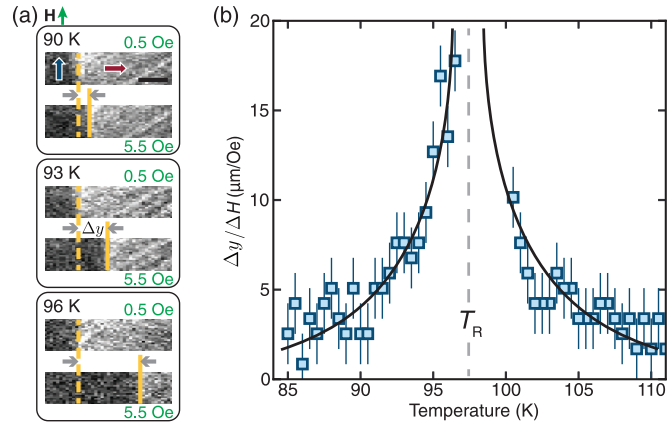

FIG. 4. Divergence of the domain wall susceptibility. (a) SHG images displaying domain wall movement Δy, when H increases from 0.5 to 5.5 Oe ($\Delta H = 5$ Oe) at three different temperatures. Yellow dashed and solid vertical lines mark domain wall positions at 0.5 and 5.5 Oe, respectively. Scale bar, 40 μm. Vertical pixel sizes are compressed twofold and images are rotated 90° clockwise relative to other figures. (b) Temperature dependence of domain wall motion per change in H field around T_R. Black lines are guides to the eye. Error bars are determined by uncertainty in domain wall horizontal positions.

position (Δy) of the 90° domain wall when H is varied from 0.5 to 5.5 Oe along the x direction. As the temperature varies from 90 to 96 K, ΔH has an increasingly large effect on domain wall motion. Since wall motion along y is nearly uniform, the change in magnetization along x is proportional to Δy, hence, $\Delta y/\Delta H$ measures domain wall susceptibility. By repeating this experiment at many temperatures, we identify a striking divergence in the domain wall susceptibility at T_R, consistent with conclusions drawn from low-field magnetometry [7,27]. As the net uniaxial anisotropy crosses zero, 90° domain walls become energetically unfavorable and are easily expelled by small H. High domain wall tunability near T_R may be leveraged to prepare large AFM domains of a desired orientation [27,42].

Our approach to locally readout AFM states, globally image AFM domain walls, and deterministically switch 90° domains in a cuprate Mott insulator augments existing AFM detection and manipulation schemes in other material classes, such as magnetoelectric oxides, rare-earth orthoferrites, and metallic alloys [43]. Temperature-tunable anisotropy may be valuable for domain wall engineering, spin-superfluidity experiments [44], and studies of intrinsic domain wall mobility [45–47]. Because $Sr_2Cu_3O_4Cl_2$ is sensitive to small changes in the microscopic parameters, especially around T_R, it may be amenable to AFM manipulation with various other techniques, including strain tuning and nonthermal optical control [48].

We acknowledge helpful conversations with D. Silevitch and P. Lee. The SHG measurements were supported by an ARO PECASE Award No. W911NF-17-1-0204. D.H. also acknowledges support for instrumentation from the David and Lucile Packard Foundation and from the Institute for Quantum Information and Matter (IQIM), an NSF Physics Frontiers Center (Grant No. PHY-1733907). K.L.S. acknowledges a Caltech Prize Postdoctoral Fellowship. A.R thanks the Zuckerman Foundation, and the Israel Science Foundation (Grant No. 1017/20). The work at Stanford and SLAC (crystal growth and sample characterization) was supported by the U.S. Department of Energy (DOE), Office of Science, Basic Energy Sciences, Materials Sciences and Engineering Division, under Contract No. DE-AC02-76SF00515.

[1] T. Jungwirth, X. Marti, P. Wadley, and J. Wunderlich, Antiferromagnetic spintronics, Nat. Nanotechnol. **11**, 231 (2016).
[2] V. Baltz, A. Manchon, M. Tsoi, T. Moriyama, T. Ono, and Y. Tserkovnyak, Antiferromagnetic spintronics, Rev. Mod. Phys. **90**, 015005 (2018).
[3] P. Němec, M. Fiebig, T. Kampfrath, and A. V. Kimel, Antiferromagnetic opto-spintronics, Nat. Phys. **14**, 229 (2018).
[4] O. Gomonay, V. Baltz, A. Brataas, and Y. Tserkovnyak, Antiferromagnetic spin textures and dynamics, Nat. Phys. **14**, 213 (2018).
[5] E. Manousakis, The spin-1/2 Heisenberg antiferromagnet on a square lattice and its application to the cuprous oxides, Rev. Mod. Phys. **63**, 1 (1991).
[6] P. A. Lee, N. Nagaosa, and X.-G. Wen, Doping a Mott insulator: Physics of high-temperature superconductivity, Rev. Mod. Phys. **78**, 17 (2006).
[7] B. Parks, M. A. Kastner, Y. J. Kim, A. B. Harris, F. C. Chou, O. Entin-Wohlman, and A. Aharony, Magnetization measurements of antiferromagnetic domains in $Sr_2Cu_3O_4Cl_2$, Phys. Rev. B **63**, 134433 (2001).
[8] B. Náfrádi, T. Keller, F. Hardy, C. Meingast, A. Erb, and B. Keimer, Magnetostriction and Magnetostructural Domains in Antiferromagnetic $YBa_2CU_3O_6$, Phys. Rev. Lett. **116**, 047001 (2016).
[9] M. Fiebig, V. V. Pavlov, and R. V. Pisarev, Second-harmonic generation as a tool for studying electronic and magnetic structures of crystals, J. Opt. Soc. Am. B **22**, 96 (2005).
[10] A. Kirilyuk and T. Rasing, Magnetization-induced-second-harmonic generation from surfaces and interfaces, J. Opt. Soc. Am. B **22**, 148 (2005).
[11] S.-W. Cheong, M. Fiebig, W. Wu, L. Chapon, and V. Kiryukhin, Seeing is believing: visualization of antiferromagnetic domains, npj Quantum Mater. **5**, 3 (2020).
[12] M. Fiebig, N. P. Duong, T. Satoh, B. B. Van Aken, K. Miyano, Y. Tomioka, and Y. Tokura, Ultrafast magnetization dynamics of antiferromagnetic compounds, J. Phys. D: Appl. Phys. **41**, 164005 (2008).
[13] J.-Y. Chauleau, E. Haltz, C. Carrétéro, S. Fusil, and M. Viret, Multi-stimuli manipulation of antiferromagnetic domains assessed by second-harmonic imaging, Nat. Mater. **16**, 803 (2017).
[14] C. Tzschaschel, T. Satoh, and M. Fiebig, Tracking the ultrafast motion of an antiferromagnetic order parameter, Nat. Commun. **10**, 3995 (2019).
[15] Z. Sun, Y. Yi, T. Song, G. Clark, B. Huang, Y. Shan, S. Wu, D. Huang, C. Gao, Z. Chen, M. McGuire, T. Cao, D. Xiao, W.-T. Liu, W. Yao, X. Xu, and S. Wu, Giant nonreciprocal second-harmonic generation from antiferromagnetic bilayer CrI_3, Nature (London) **572**, 497 (2019).
[16] H. Chu, C. J. Roh, J. O. Island, C. Li, S. Lee, J. Chen, J.-G. Park, A. F. Young, J. S. Lee, and D. Hsieh, Linear Magnetoelectric Phase in Ultrathin $MnPS_3$ Probed by Optical Second Harmonic Generation, Phys. Rev. Lett. **124**, 027601 (2020).
[17] B. Kaminski, M. Lafrentz, R. V. Pisarev, D. R. Yakovlev, V. V. Pavlov, V. A. Lukoshkin, A. B. Henriques, G. Springholz, G. Bauer, E. Abramof, P. H. O. Rappl, and M. Bayer, Spin-Induced Optical Second Harmonic Generation in the Centrosymmetric Magnetic Semiconductors EuTe and EuSe, Phys. Rev. Lett. **103**, 057203 (2009).
[18] M. Matsubara, A. Schmehl, J. Mannhart, D. G. Schlom, and M. Fiebig, Large nonlinear magneto-optical effect in the centrosymmetric ferromagnetic semiconductor EuO, Phys. Rev. B **81**, 214447 (2010).
[19] A. de la Torre, K. L. Seyler, L. Zhao, S. D. Matteo, M. S. Scheurer, Y. Li, B. Yu, M. Greven, S. Sachdev, M. R. Norman, and D. Hsieh, Mirror symmetry breaking in a model insulating cuprate, Nat. Phys. **17**, 777 (2021).
[20] A. de la Torre, S. Di Matteo, D. Hsieh, and M. R. Norman, Implications of second harmonic generation for hidden order in $Sr_2CuO_2Cl_2$, Phys. Rev. B **104**, 035138 (2021).

[21] B. Grande and H. Müller-Buschbaum, Über oxocuprate, XIV zur kristallchemie von $Sr_2Cu_3O_4Cl_2$, Z. Naturforschung. B **31**, 405 (1976).

[22] K. Yamada, N. Suzuki, and J. Akimitsu, Magnetic properties of $(Sr,Ba)_2Cu_3O_4Cl_2$: Two-dimensional antiferromagnetic cuprates containing two types of Cu-site, Phys. B (Amsterdam) **213-214**, 191 (1995).

[23] F. C. Chou, A. Aharony, R. J. Birgeneau, O. Entin-Wohlman, M. Greven, A. B. Harris, M. A. Kastner, Y. J. Kim, D. S. Kleinberg, Y. S. Lee, and Q. Zhu, Ferromagnetic Moment and Spin Rotation Transitions in Tetragonal Antiferromagnetic $Sr_2Cu_3O_4Cl_2$, Phys. Rev. Lett. **78**, 535 (1997).

[24] M. A. Kastner, A. Aharony, R. J. Birgeneau, F. C. Chou, O. Entin-Wohlman, M. Greven, A. B. Harris, Y. J. Kim, Y. S. Lee, M. E. Parks, and Q. Zhu, Field-dependent antiferromagnetism and ferromagnetism of the two copper sublattices in $Sr_2Cu_3O_4Cl_2$, Phys. Rev. B **59**, 14702 (1999).

[25] H. V. Gomonay, I. G. Korniienko, and V. M. Loktev, Theory of magnetization in multiferroics: Competition between ferromagnetic and antiferromagnetic domains, Phys. Rev. B **83**, 054424 (2011).

[26] J. W. Harter, L. Niu, A. J. Woss, and D. Hsieh, High-speed measurement of rotational anisotropy nonlinear optical harmonic generation using position-sensitive detection, Opt. Lett. **40**, 4671 (2015).

[27] See Supplemental Material at http://link.aps.org/supplemental/10.1103/PhysRevB.106.L140403 for further details of the experimental methods and supporting data, which includes Refs. [28–31].

[28] S. Noro, T. Kouchi, H. Harada, T. Yamadaya, M. Tadokoro, and H. Suzuki, Magnetic properties of $Ba_2Cu_3O_4Cl_2$ single crystals, Mater. Sci. Eng. B **25**, 167 (1994).

[29] R. R. Birss, *Symmetry and Magnetism* (North-Holland, Amsterdam, 1964)

[30] J. Reif, J. C. Zink, C.-M. Schneider, and J. Kirschner, Effects of Surface Magnetism on Optical Second Harmonic Generation, Phys. Rev. Lett. **67**, 2878 (1991).

[31] H. V. Gomonay and V. M. Loktev, Shape-induced phenomena in finite-size antiferromagnets, Phys. Rev. B **75**, 174439 (2007).

[32] Y. J. Kim, R. J. Birgeneau, F. C. Chou, M. Greven, M. A. Kastner, Y. S. Lee, B. O. Wells, A. Aharony, O. Entin-Wohlman, I. Y. Korenblit, A. B. Harris, R. W. Erwin, and G. Shirane, Neutron scattering study of $Sr_2Cu_3O_4Cl_2$, Phys. Rev. B **64**, 024435 (2001).

[33] K. L. Seyler, A. de la Torre, Z. Porter, E. Zoghlin, R. Polski, M. Nguyen, S. Nadj-Perge, S. D. Wilson, and D. Hsieh, Spin-orbit-enhanced magnetic surface second-harmonic generation in Sr_2IrO_4, Phys. Rev. B **102**, 201113(R) (2020).

[34] T. Yildirim, A. B. Harris, A. Aharony, and O. Entin-Wohlman, Anisotropic spin hamiltonians due to spin-orbit and coulomb exchange interactions, Phys. Rev. B **52**, 10239 (1995).

[35] J. Liu, H.-J. Koo, H. Xiang, R. K. Kremer, and M.-H. Whangbo, Most spin-1/2 transition-metal ions do have single ion anisotropy, J. Chem. Phys. **141**, 124113 (2014).

[36] L. R. Bickford, Ferromagnetic resonance absorption in magnetite single crystals, Phys. Rev. **78**, 449 (1950).

[37] L. Martín-García, A. Mascaraque, B. M. Pabón, R. Bliem, G. S. Parkinson, G. Chen, A. K. Schmid, and J. de la Figuera, Spin reorientation transition of magnetite (001), Phys. Rev. B **93**, 134419 (2016).

[38] F. J. Morin, Magnetic susceptibility of αFe_2O_3 and αFe_2O_3 with added titanium, Phys. Rev. **78**, 819 (1950).

[39] A. Broese van Groenou, P. F. Bongers, and A. L. Stuyts, Magnetism, microstructure and crystal chemistry of spinel ferrites, Mater. Sci. Eng. **3**, 317 (1969).

[40] J. O. Artman, J. C. Murphy, and S. Foner, Magnetic anisotropy in antiferromagnetic corundum-type sesquioxides, Phys. Rev. **138**, A912 (1965).

[41] K. P. Belov, A. K. Zvezdin, A. M. Kadomtseva, and R. Z. Levitin, Spin-reorientation transitions in rare-earth magnets, Sov. Phys.–Usp. **19**, 574 (1976).

[42] O. Gomonay and D. Bossini, Linear and nonlinear spin dynamics in multi-domain magnetoelastic antiferromagnets, J. Phys. D: Appl. Phys. **54**, 374004 (2021).

[43] C. Song, Y. You, X. Chen, X. Zhou, Y. Wang, and F. Pan, How to manipulate magnetic states of antiferromagnets, Nanotechnology **29**, 112001 (2018).

[44] E. B. Sonin, Spin currents and spin superfluidity, Adv. Phys. **59**, 181 (2010).

[45] L. Thomas, M. Hayashi, X. Jiang, R. Moriya, C. Rettner, and S. Parkin, Resonant amplification of magnetic domain-wall motion by a train of current pulses, Science **315**, 1553 (2007).

[46] K.-J. Kim, S. K. Kim, Y. Hirata, S.-H. Oh, T. Tono, D.-H. Kim, T. Okuno, W. S. Ham, S. Kim, G. Go, Y. Tserkovnyak, A. Tsukamoto, T. Moriyama, K.-J. Lee, and T. Ono, Fast domain wall motion in the vicinity of the angular momentum compensation temperature of ferrimagnets, Nat. Mater. **16**, 1187 (2017).

[47] L. Caretta, M. Mann, F. Büttner, K. Ueda, B. Pfau, C. M. Günther, P. Hessing, A. Churikova, C. Klose, M. Schneider, D. Engel, C. Marcus, D. Bono, K. Bagschik, S. Eisebitt, and G. S. D. Beach, Fast current-driven domain walls and small skyrmions in a compensated ferrimagnet, Nat. Nanotechnol. **13**, 1154 (2018).

[48] A. de la Torre, D. M. Kennes, M. Claassen, S. Gerber, J. W. McIver, and M. A. Sentef, Colloquium: Nonthermal pathways to ultrafast control in quantum materials, Rev. Mod. Phys. **93**, 041002 (2021).